Solar Energy Materials and Solar Cells 172 (2017) 117–123

Contents lists available at ScienceDirect

Solar Energy Materials and Solar Cells

journal homepage: www.elsevier.com/locate/solmat

A broadband Pb-chalcogenide/CdS solar cells with tandem quantum-dots embedded in the bulk matrix (QDiM) absorption layers by using chemical bath deposition

Jijun Qiu[a,b,*], Binbin Weng[a,1], Wanyin Ge[a], Lance L. McDowell[a], Zhihua Cai[a,b], Zhisheng Shi[a,**]

[a] School of Electrical and Computer Engineering, University of Oklahoma, Norman, OK 73019, USA
[b] Nanolight, Inc., Norman, OK 73069, USA

ARTICLE INFO

Keywords:
PbSe
Solar cells
Quantum dots embedded in the bulk matrix (QDiM)
Tandam
Chemical bath deposition (CBD)

ABSTRACT

In this paper we have presented a power conversion efficiency (PCE) enhanced Pb-chalcogenide/CdS quantum dots (QDs) solar cells with novel tandem absorption layers synthesized by using chemical bath deposition (CBD) method. The tandem absorption layer is assembled by orderly stacking PbS-QDs layer, PbS-QDiM layer and PbSe-QDiM layer. Compared to single layer PbS-QDs/CdS solar cells, the solar cell with double-tandem layers (PbS-QDiM/QDs) shows the highest short current density (J_{sc}) of 47.5 mA/cm^2 due to smoothing of the photo-generated carrier transportation and enhancing the absorption in the visible region 530–800 nm. However, the decreased open circuit voltage (V_{oc}) of 0.14 eV results in a low power conversion efficiency (PCE) of 2.2%. The triple-tandem absorber (PbSe-QDiM/PbS-QDiM/QDs) enhances the spectra absorption both in the visible (500–800 nm) and near-infrared (1000–1700 nm) regions, resulting in a higher short current density (J_{sc}) of 40 mA/cm^2, while keeping a relatively large open circuit voltage (V_{oc}) of 0.28 eV. Through an architectural modification, an enhancement of power conversion efficiency (PCE) of 4.2% has been achieved.

1. Introduction

In recent years intensive studies have been carried out in lead chalcogenide (PbX) materials in attempt to explore their potential applications in optoelectronics [1–3] and photovoltaics [4–10]. As promising constituent materials for solar cells in Fig. 1(a) [4–10], PbS colloid quantum dots (CQDs), which are synthesized by high temperature injection method, have been gaining much attention due to their unique optoelectronic properties. The high absorption cross section and CQD sized related tunable band gap, which is caused by the quantum confinement effect, enable efficient capture of solar illumination. Multiple exitron generation effect could overcome the efficiency limit of single energy gap to improve the light-to-current conversion efficiencies. By using the PbS CQD, the power conversion efficiency (PCE) of 9.2% has been demonstrated recently [10].

With an in-depth study on fundamental physical principles [4,11,12] it is found that the key factor limiting PCE of CQDs solar cells is mainly attributed to their inefficient extraction of photon-generated carriers. Such inefficiency is the result of the introduction of organic ligand, which led to a low short circuit current (J_{sc}) generally less than 30 mA/cm^2.

It has been demonstrated that this limitation is gradually being overcome by the material-engineering and the architecture-engineering [4]. The goal of the material-engineering is to reduce the density of trap centers, improve the transport properties of the carriers, and reduce the extent of energy level pinning, which could be realized by selecting and optimizing the synthesis strategies, passivating QDs through the ligand exchange, and modifying QDs through the core-shell strategies or surface self-healing. The goal of the architecture-engineering is to capture a wider spectrum of the incident light and improve the transportation of the photo-generated carriers. The evolution of the device architectures has undergone from the Schottky structure to the heterojunction, and then to multi-junction tandem integration.

In this paper, a novel structure of IV-VI materials with QD embedded in the bulk material matrix (QDiM) was developed. Based on the physical properties of the QDiM structure, two types of the stacked tandem architectures, showing in Fig. 1(b) and (c), were proposed to increase the performance of traditional PbS-QDs solar cells. Through optimizing the thickness of every absorber layer, the best tandem QDs solar cell devices we developed demonstrated a PCE of 4.2%, which is

* Corresponding author at: School of Electrical and Computer Engineering, University of Oklahoma, Norman, OK 73019, USA.
** Corresponding author.
E-mail addresses: jjqiu@ou.edu (J. Qiu), shi@ou.edu (Z. Shi).
[1] Jijun Qiu and Binbin Weng contributed equally to this work.

http://dx.doi.org/10.1016/j.solmat.2017.07.025
Received 24 April 2017; Received in revised form 16 June 2017; Accepted 18 July 2017
Available online 25 July 2017
0927-0248/

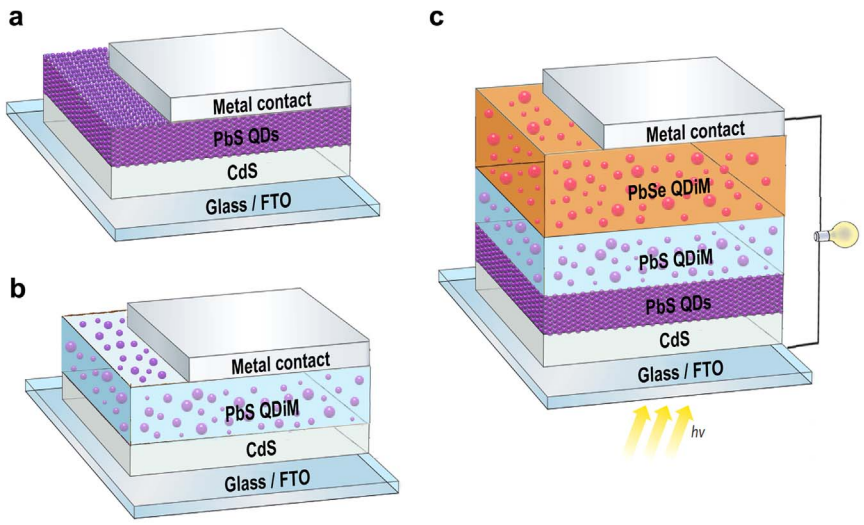

Fig. 1. Schematic illustration of CBD-PbS/CdS solar cells with different assembled structures. (a) Traditional PbS-QDs/CdS solar cell, (b) PbS-QDiM/QDs/CdS stacked tandem two-layer solar cell and (c) PbSe-QDiM /PbS-QDiM/QDs/CdS stacked tandem triple-layer solar cell.

higher than the reported results by Hernandez-Borja (1.63%) [13], Obaid (1.68%) [14] and Cho (3.10% and 4.03%) [15,16]. In addition, we found that the QDiM layers can also improve the stability of the solar cell devices.

2. Experimental details

All chemicals used in the experiment were analytic grade reagents without further purification, *and a scheme for preparing the tandem layer was shown in* Fig. 2.

2.1. Materials growth and device fabrication

CdS films were grown on the fluorine doped tin oxide (FTO) substrates by using the chemical bath deposition (CBD) method. An aqueous precursor was prepared by mixing 8 mM cadmium acetate ($Cd(CH_3CO_2)_2$), 8 mM ammonium acetate ($NH_4CH_3CO_2$), 12 mM thiourea (CH_4N_2S), and 2 M ammonium hydroxide ($NH3{\cdot}H_2O$, 28%). The cleaned substrates were immersed into the precursor with FTO facing down. The solution was then heated up and stabilized for 1 h in the 80 °C water bath to obtain a thin film with the thickness of 300 nm.

Both of PbS-QDs films and PbS-QDiM films were deposited from the precursor mixed with lead acetate ($Pb(C_2H_3O_2)_2$), sodium hydroxide (NaOH), thiourea (CH_4N_2S) and triethanolamine ($C_6H_{15}NO_3$, abbreviated as TEA). This procedure was optimized for PbS growth on CdS coated FTO substrates and glass substrates. The final composition of the deposition solution for PbS QDs was: 120 mM NaOH, 10 mM Pb $(C_2H_3O_2)_2$, 45 mM $C_6H_{15}NO_3$ and 10 mM CH_4N_2S, mixed in this order. Therefore, the CdS coated FTO substrates (or glass substrates) were placed with the CdS facing down in the solution, mounted on a custom-designed Teflon stage at an angle of 70° with respect to the surface. The growth was carried out at a low temperature (typical 3–5 °C) for 72 h for 300 nm thickness. The QDiM-PbS films were deposited at a high temperature (typical 25 °C) from a composited precursor of 0.3 M NaOH, 25 mM $Pb(C_2H_3O_2)_2$, 90 mM $C_6H_{15}NO$ and 50 mM CH_4N_2S. The desired thickness was obtained by refreshing the precursor every hour, which results in an increase of thickness of 200 nm/per circle.

PbSe-QDiM films were synthesized from an aqueous precursor containing NaOH, $Pb(C_2H_3O_2)_2$, selenosulfate (Na_2SeSO_3) and TEA with a concentration ratio of 12:1:1:0.2. The resultant substrates were

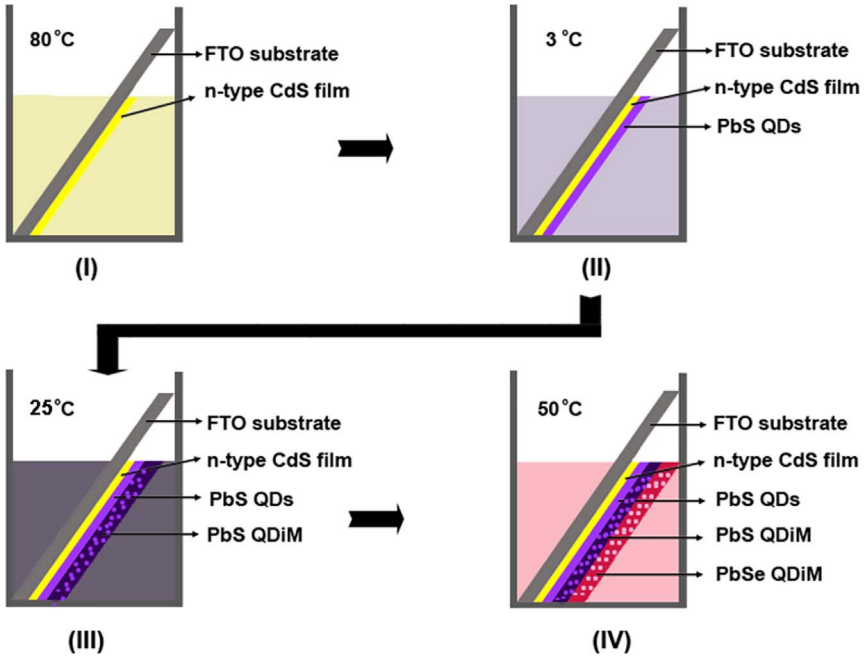

Fig. 2. Schematic illustration of fabrication processing for tandem absorption layer by chemical bath deposition. (a) The deposition of n-type CdS films; (b) P-type PbS-QDs deposition over the CdS film; (c) PbS-QDiM deposition over the PbS-QDs/CdS and (d) PbSe-QDiM deposition over PbS-QDiM/QDs/CdS.

immersed upside-down into the precursor and maintained at 50 °C with a growth rate of 300 nm/h.

For the solar cell devices, a small segment of the PbSe-QDiM/PbS-QDiM/QDs/CdS film on one edge of the sample was wet-chemically etched by using 10% hydrochloric HCl to expose the bottom contact layer, FTO. Then Au electrode was deposited by the thermal evaporation method, and a shadow-mask was used to form the electrode pattern. The active area of the device was 0.1 cm^2 defined by the overlay of Au.

2.2. Structure and morphology, optoelectronic and device characterizations

The morphologies of the synthesized thin films were examined by a Zeiss Neon-40 EsB high resolution field-emission scanning electron microscope (FESEM). Hall Effect measurements were conducted in Van der Pauw four-point probe configuration, using fresh indium contacts, in an automated EGK HEM-2000, with a magnetic induction of 0.37 T. The visible-NIR PL spectrum was conducted by Princeton Instruments acton sp2500 monochromater with 325 nm He-Cd continuous laser, while the IR PL spectrum were characterized by a Fourier transform infrared (FTIR) spectrometer in Step-Scan mode with a 1.064 μm Q-switched Nd:YAG pulse pumping laser (5 ns, 10 Hz). The external quantum efficiency (EQE) was analyzed using the FTIR with Si and Ge detectors. The transmission spectra of the samples were measured by the FTIR system with Si detector for 350–1000 nm and DLATGS detector for 1–10 μm. The Current density-voltage (J-V) behavior was examined by using a current-voltage analyzer and a solar simulator (Oriel Sol2A Solar simulator) under AM 1.5G (100 mW/cm^2). A copper mask was attached to the solar cell with an aperture with an area of 0.1 cm^2 to define the active area of the devices.

3. Results and discussions

It is well known[17–22] that the structural morphology of chalcogenide semiconductor films could be finely tailored by the CBD processing parameters, such as complex agents, complex/Pb ratio, pH value and growth temperature. Fig. 3 shows the different structural morphologies of the PbS and PbSe films, resulting from the control of the complex agent and the growth temperature.

The PbS thin film synthesized from the lowest growth temperature of 3 °C appears to be highly adhesive, light brown in color, surface-smooth, uniform and reflecting. The top-view FESEM image in Fig. 3(a) reveals the formation of a nanostructured thin film with homogeneous, nearly spherical and fine-grained morphology without the presence of cracks. The side-view FESEM image in Fig. 3(b) clearly reveals that the film is made up of aggregates of individual small crystallites of 6–8 nm in diameter without any voids, and the crystallite size is fairly constant throughout the thickness.

With increasing the growth temperatures, the color of PbS films gradually deepen to brownish black, then to grey, as shown in the Supporting information Fig. S1. At the same time, the transparency quickly declines to opacity as temperature was increased to 10 °C. The top-view FESEM image in Fig. 3(c) shows that cube-like particles with 0.2 μm are formed as the temperature ramped up to 10 °C. The particle size is found to continuously increase to 0.5–0.8 μm with increasing the growth temperature from 10 to 30 °C, as shown in Fig. 3(e), making them much rougher, resulting in much stronger light scattering. The size distribution of the crystallites can be seen to be rather broad.

The large magnification cross-side view FESEM images in Fig. 3(f) and (g) show that every micron-size cubic-like crystallite is made up of very individual small crystallites of 10–12 nm surrounded by a non-nanostructure matrix. Similar structures and structural changes are observed from the PbSe growth, dependent on complex agent and temperature, as shown in Fig. 3 from (h) to (K).

Such a structure of individual nano-crystallites embedded in a micro-size cubic-shaped matrix (QDiM) was further confirmed by the appearance of multiple PL emission peaks, shown in Fig. 4. Only one strong peak at 2.3 eV was observed in the PbS-QDs absorber fabricated at 3 °C. This blue shift of the band gap towards the visible range indicates that the film consists of small QDs with uniform size distribution. However, three PL emission peaks were observed from the films fabricated at 25 °C at the wavelength range from 400 to 3000 nm. Two strong normalized peaks at 0.47 and 2.3 eV are attributed to the emissions of micro-crystal and PbS-QDs particles, respectively. The broad and weak peak centred at 1.1 eV could be originated from a small amount of relatively large QDs with inhomogeneous sizes. Four strong peaks at 0.72, 0.6, 0.38 and 0.32 eV were observed from the PbSe-QDiM PL spectrum. The first three peaks were attributed to the emissions of PbSe quantum dots in the matrix due to the blue shift relative to the one at 0.32 eV which as emitted from the micro PbSe matrix. Meanwhile, these three peaks covering the wavelength range from 1.7 to 3.2 μm, indicates that the size of PbSe-QDs is inhomogeneous.

Such a QDiM morphology evidently confirms the latest speculation of Prof. Y. Golan in 2016 [18]. We believe that the QDiM growth process is dominated by the ion-by-ion mechanism along with the cluster-by-cluster mechanism, due to a prolonged transition time caused by the introduction of the high concentration TEA.

It is well known that the role of the complex agents [18–22] is to bind with the metal ions to prevent rapid precipitation through the homogeneous reaction. TEA can effectively complex Pb^{2+} in the solution, and allow the slow release of the free Pb^{2+} to react with the anion generated slowly at lower temperature (< 5 °C). Therefore, a QDs film forms by adsorption, migration and coagulation of colloidal nano-particles pre-formed in the solution by a homogeneous reaction in a low growth rate. This process is commonly known as the cluster-by-cluster mechanism.

The increase of growth temperature significantly accelerates the release rates of lead-complex and anion (S^{2-} and Se^{2-}), resulting in a switch from the initial cluster mechanism to the ion-by-ion mechanism. These high concentration ions directly condense at the reacting surface and form the film by a heterogeneous precipitation. Because of the transition from the cluster-by-cluster to the ion-by-ion mechanism, these initial round-shaped clusters on the substrate can develop into (100) faceted cube-shaped micro-crystallites by a thermodynamically driven regime.

However, due to the high TEA:Pb ratio concentration in our case, the mechanism transition process could take longer time in the interval range of 60–120 min [18]. In the course of the prolonged transition, both process may coexist and interact, leading to films where small colloids are embedded in the faceted micro-crystals. At the same time, the cluster process can still survive in the dominated ion-by-ion mechanism due to a low anion (S or Se) concentration and a short deposition time in this work [18].

Table 1 represents the carrier concentration and mobility dependent on the growth temperature. These results were obtained by the Hall measurement. All samples show the p-type conductivity. Increasing the deposition temperature from 3 to 25 °C results in the decrease of the PbS carrier concentration from 5.5×10^{18} to 2×10^{17} cm^{-3}, and the increase of the carrier mobility from 0.9 to 13 cm^2/V s. A similar variation trend was also observed from the PbSe films. Similar results were reported by Cho [15]. The decreased concentration is mainly attributed to the decreased S/Pb ratio in PbS films with the increased temperatures [15]. At the same time, roughened interfaces and the discontinued particles, as shown in Fig. 3, impede the carrier transport process. The increased mobility is due to the improved crystal quality (less defeats) and the decreased grain boundaries at a higher growth temperature.

The typical cross-side view FESEM images of the PbS-QDs/CdS and the PbS-QDiM/CdS solar cells are presented in Fig. 5(a) and (b). Fig. 6 shows their typical current density–voltage characteristics. The best photovoltaic performance of the devices with the optimized absorption layer thickness is demonstrated in Table 2, including the short circuit current density (J_{sc}), the open circuit voltage (V_{oc}), the fill factor (FF)

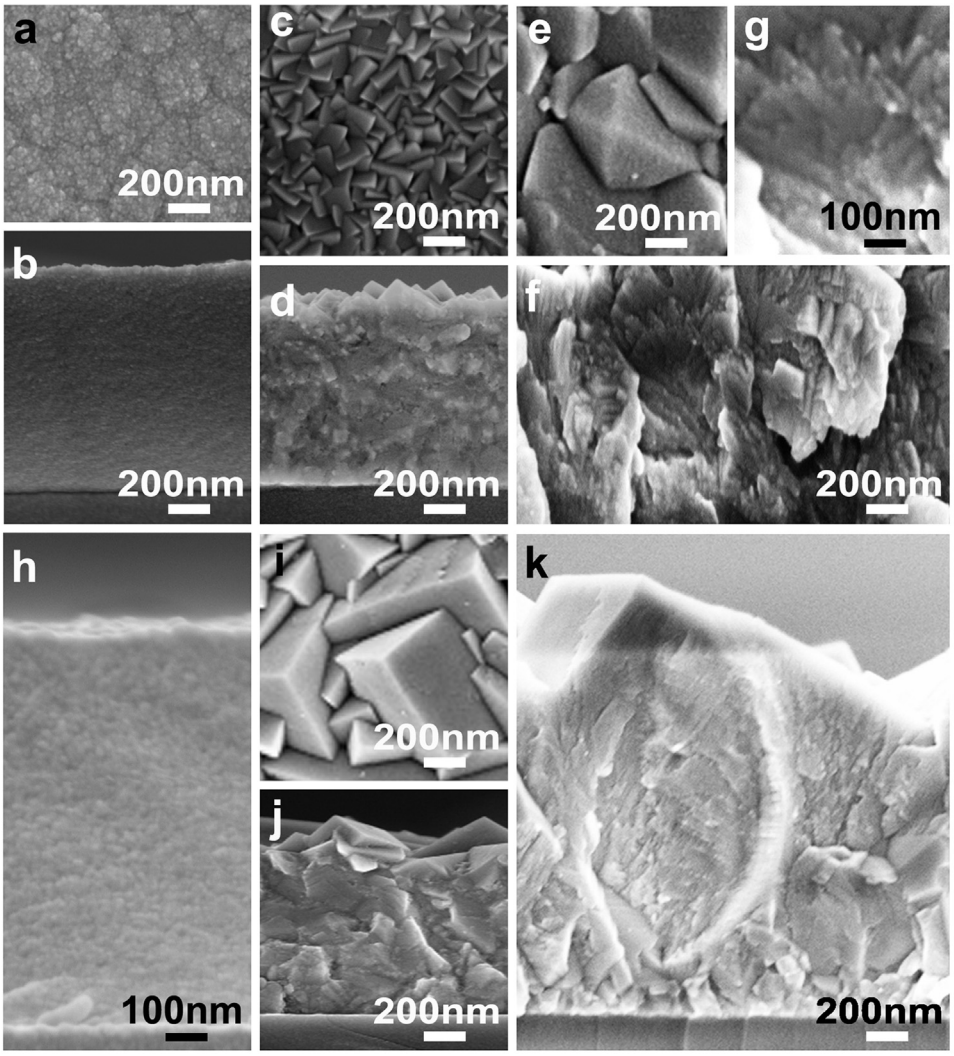

Fig. 3. Typical morphologies of PbS and PbSe films fabricated from various growth temperatures. Top- and side- view FESEM images of PbS films obtained from (a), (b) 3 °C, (c), (d) 10 °C and (e), (f) and (g) 25 °C. Side-and top-view FESEM images of PbSe films obtained from (h) 3 °C, (i), (j) 25 °C and (k) 80 °C.

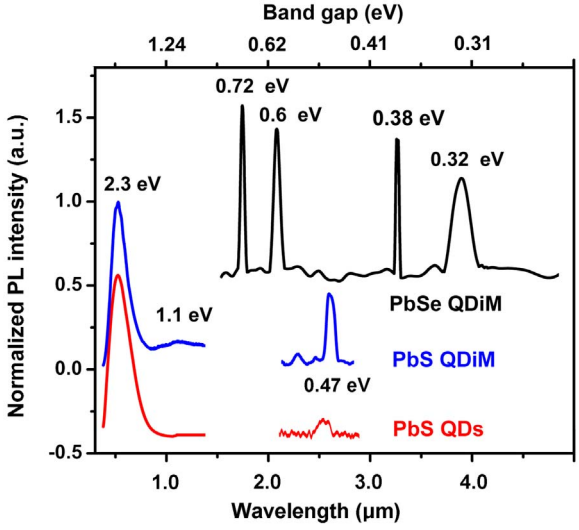

Fig. 4. Typical PL spectra of PbS-QDs films and PbS-QDiM and PbSe-QDiM morphologies which were fabricated from growth temperature of 3, 25 and 50 °C, respectively.

and the power conversion efficiency (PCE). The influence of the thickness will be discussed later in this work. In the PbS-QDs/CdS device, a large open circuit voltage (V_{oc}) of 0.32 V was achieved. However, the J_{sc} is only 5 mA/cm^2, leading a lower PCE of 0.6%. Therefore, the PbS-QDiM/CdS structure was then proposed to improve the J_{sc}.

Table 1
Electrical properties of PbS and PbSe films with QDs and QDiM morphologies which fabricated from various growth temperatures.

	PbS		PbSe	
	QDs	QDiM	QDs	QDiM
Carrier concentration ($\times 10^{18}$ cm^{-3})	5.5	0.2	3.2	0.4
Mobility (cm/V s)	0.9	13	1.4	11

As shown in Table 2, this new device achieved a largely improved J_{sc} of 47.5 mA/cm^2. To our knowledge, this is the largest value ever reported, and results in a PCE of 2.2%. Because of the higher carrier mobility and the lower defect density in the micro-size matrix crystals, the photo induced carrier generated from QDs absorption can transport through the thin film much easier. On the other hand, the external quantum efficiency EQE in Fig. 7 shows a broader spectral absorption and a higher EQE. For the PbS-QDs/CdS solar cell, the generated photocurrent is mainly attributed to the absorption in the visible region 530–800 nm. However, for the modified PbS-QDiM/CdS solar cell, besides of an enhanced absorption in the visible region (higher EQE), an obvious near infrared absorption region from 1.0 to 1.3 μm was also clearly observed, which explains the strong enhancement of the J_{sc} by 10 times.

On the other hand, it is noticed from the Fig. 6 that the PbS-QDiM/

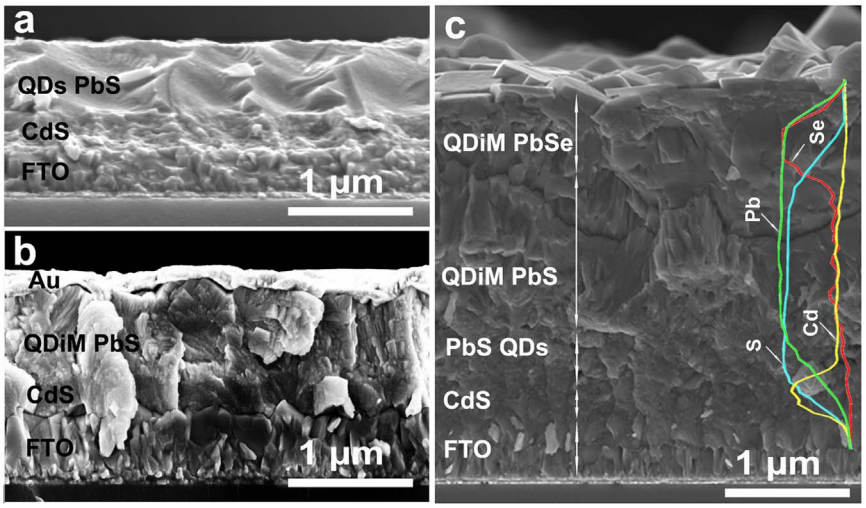

Fig. 5. Typical side-view FESEM images of CBD-PbS/CdS solar cells with different assembled structures. (a) PbS-QDs/CdS solar cell, (b) PbS-QDiM/CdS solar cell and (c) PbSe-QDiM/PbS-QDiM/QDs/CdS stacked tandem solar cell.

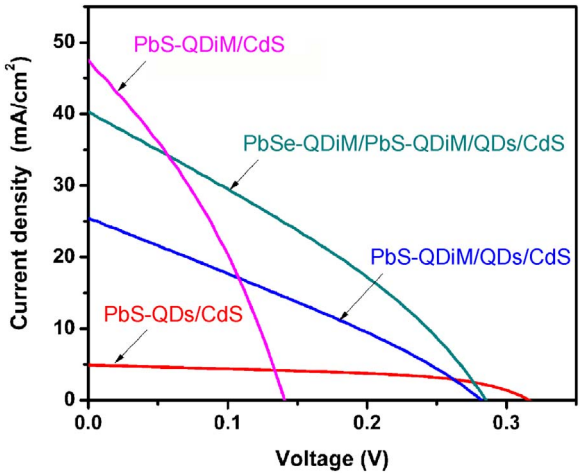

Fig. 6. The current density vs. voltage plots for CBD-PbS/CdS solar cells with different structures.

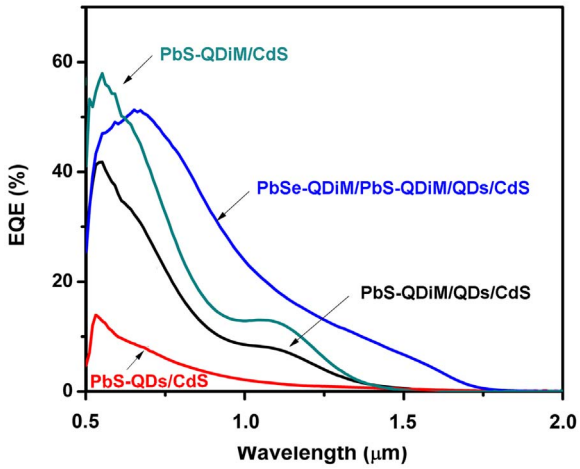

Fig. 7. EQE spectra of CBD-PbS/CdS solar cells with various assembled structures.

Table 2
The optimized photovoltaic performances of PbS/CdS solar cells with different assembled structures.

	J_{SC} (mA/cm^2)	V_{OC} (V)	*FF* (%)	*PCE* (%)	*EQE-J*$_{SC}$ (mA/cm^2)
PbS-QDs/CdS	5.0	0.32	40	0.6	2.40
PbS-QDiM/CdS	47.5	0.14	33	2.2	15.1
PbS-QDiM/QDs/CdS	25.5	0.28	32	2.3	10.0
PbSe-QDiM/PbS-QDiM/QDs/CdS	40	0.28	38	4.2	17.2

CdS solar cell, presents a significant power losses through the decreased V_{oc} from 0.32 to 0.14 eV as well as the increased current-voltage slope compared with the original PbS-QD/CdS solar cell. Firstly, one of the reasons could be due to the decreased shunt resistance, which provides an alternate current path for the light-generated current. Such a diversion reduces the amount of current flowing through the solar cell junction and also reduces the voltage generated from the solar cell. Such leakage is also facilitated by the dark current-voltage characterization chart shown in the Supporting information Fig. S2. Typically, the reduced shunt resistance is due to the defects introduced through the fabrication process rather than poor solar cell design, which means the issue can be solved. However, in this work, the deficiency caused the leakage in the process has not been targeted yet. Further investigation will be made specifically on it in our future work.

Furthermore, we believe that the decreased V_{oc} might be also caused by the increased particle size from ~ 8 nm of QDs to the micro-scale of QDiM. The V_{oc} is intrinsically determined by the Fermi-energy difference and the band offset of the heterojunction materials. With increasing the particle size, the PbS band gap decreases due to the weakened quantum confinement efficiency. Consequently, band offset decreases, resulting in a significantly dropped V_{oc}. Therefore, a new structure with an inserted PbS-QDs layer in the PbS-QDiM/CdS was designed to solve this issue. This PbS-QDs layer has a larger band gap, which will rise the band offset with the CdS hole-block layer, and then increase the V_{oc}.

The structure of the sacked tandem PbS-QDiM/QDs/CdS solar cell is shown in Fig. 1(b). Compared to a single QDiM layer, the QDiM/QDs two stacked layers shows a large improvement of the V_{oc} from 0.14 to 0.28 V. However, an obvious decrease of the J_{sc} from 47.6 to 25 mA/cm^2 was observed. We suggested that the decreased J_{sc} is a result of two reasons: Firstly, the introduction of low-temperature QDs bottom layer hinders the photo-generated carrier transport due to their high trap state densities and additional grain boundaries; Secondly, the PbS-QDs layer introduces a potential barrier at the interface between the PbS-QDs and the matrix, which possibly blocks the transport of the photo-generated electrons, as indicated as in Fig. 8. This issue could be weakened by tailoring the size of PbS-QDs, as to allow the light generated carrier across the barrier by thermionic emission effect.

On the other hand, it is found that the PCE of the sacked tandem PbS-QDiM/QDs/CdS solar cell is only 2.3%. We think broadening the spectral absorption of the device can be an effective approach to further

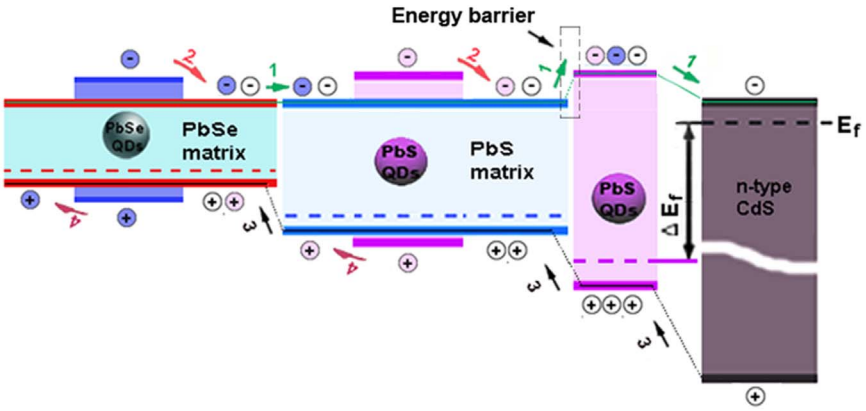

Fig. 8. The energy level diagram of PbSe-QDiM/PbS-QDiM/QDs/CdS stacked tandem solar cell structure.

improve the PCE. Therefore, A PbSe-QDiM absorption layer is introduced into the previous device to form a novel triple tandem solar cell architecture, as shown in Figs. 1(c) and 5(c). Because of a smaller band gap of 0.28 eV, and a larger Bohr radium of 46 nm [28], the quantum effect can be achieved even in the relatively large particles for PbSe material, resulting in the absorption of a much longer wavelength light. In addition, to tailor the size of the PbSe QDs is easier due to a wider growth temperature from 0 to 80 °C.

On the other hand, based on the reported electron affinities of the bulk CdS, PbS and PbSe as shown in Supporting information S3 [22–27], the energy diagram of the stacked tandem solar cell is shown in Fig. 8. Because an appropriate type-II heterojunction could be formed in the bulk p-PbSe/PbS and n-CdS at room temperature, the transportation of the photo-generated electrons and holes could be unhindered from the conductive bands (CB) and the valance bands (VB) to electrodes, respectively.

Compared to PbS-QDiM/QDs two staked layer, the PCE of the PbSe-QDiM triple-tandem stacked layer shows a significant improvement from 2.3% to 4.2%, as shown in Table 2. The enhancement was primarily due to the large increment in the J_{sc} from 25 to 40 mA/cm^2 while maintaining a large V_{oc} of 0.28 eV. It is clearly shown in Fig. 7 that, PbSe-QDiM triple-tandem stacked layer not only extends spectra response to 1.7 μm infrared region, but also exhibits a higher EQE covering a broader absorption range compared with the PbS-QDiM/QDs/CdS solar cell. Furthermore, the transmission spectrum in Fig. 9 shows that the absorption edge apparently red shift from visible to infrared area with the PbSe-QDiM layer. Therefore, the QDiM PbSe layer not only enhances the absorption of visible light, but more importantly, absorbs a larger portion of near infrared light from 1.1 to 1.7 μm. Consequently, the J_{sc} is largely improved.

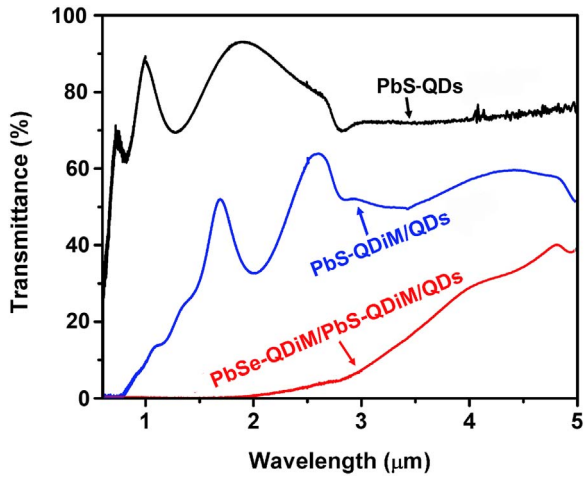

Fig. 9. Transmittance spectra of CBD-PbS/CdS solar cells with various assembled structures.

In addition, we calculated the short-circuit current by using the EQE of the cell based on the following equation:

$$J_{sc} = q \int \phi(\lambda) \cdot EQE(\lambda) d\lambda$$

where q is the charge of the electron, and ϕ is the photon flux. The calculated J_{sc} listed in the Table 2. Obviously, the EQE-J_{sc} is different with the measured directly with the I-V solar simulator.

However, the difference is not unusual. Even, for silicon solar cells, which are well understood and reproducible, there is a difference. In our case, the calculated J_{sc} is lower than J_{sc} from the I-V measurement. The two possible Explanations are shown as following [29]: (1) the light intensity from the EQE system and the solar simulator is different, which results in a various barrier for photocurrent. The barrier is large under low light intensity or monochromatic illumination (EQE), but becomes lowered at AM1.5 illumination; (2) the shunting paths can also play their role in this discrepancy of J_{sc} values. In our EQE measurement, the cell is irradiated only on a limited area of 0.01 cm^2, which is far less than the active solar cell area. Generated charge carrier can diffuse to the dark region that works as low resistance path and act as shunt for the generated current. Reducing the cell area to the area of illumination may increase the EQE.

It was found that the thickness of each absorb layer has significant influence on the performance of the stacked solar cells, as shown in Table 3. Although be favourable to the carrier transportation, ultrathin thin QDs film less than 100 nm is failed to increase the Voc possibly due to pinholes. Thinner PbS and PbSe-QDiM layers less than 1000 nm result in an inadequate absorption, and then a lower J_{sc}. Although thicker thickness, more absorption, the photo-generated carriers have higher recombination probability during travelling through thicker layers due to short diffusion lengths of the carriers, contributing a lower J_{sc} and FF, then consequent a lower PCE. The optimum thickness for the PbS-QDs,

Table 3
The effect of thickness of absorption layer on the photovoltaic performance of the stacked tandem solar cells.

	Thickness (nm)	J_{SC} (mA/cm^2)	V_{OC} (V)	***FF*** (%)	***PCE*** (%)
PbS-QDiM(1000 nm)/CdS	100	31.1	0.14	35	1.5
	200	25.5	0.28	32	2.3
	300	17.4	0.28	33	1.6
PbS-QDiM/QDs (200 nm)CdS	600	16.1	0.28	37	1.7
	800	20.5	0.28	34	1.9
	1000	25.5	0.28	32	2.3
	1200	20.2	0.28	28	1.6
PbSe-QDiM/PbS-QDiM (1000 nm)/QDs (200 nm)/CdS	600	31.2	0.28	38	3.3
	1000	40.0	0.28	38	4.2

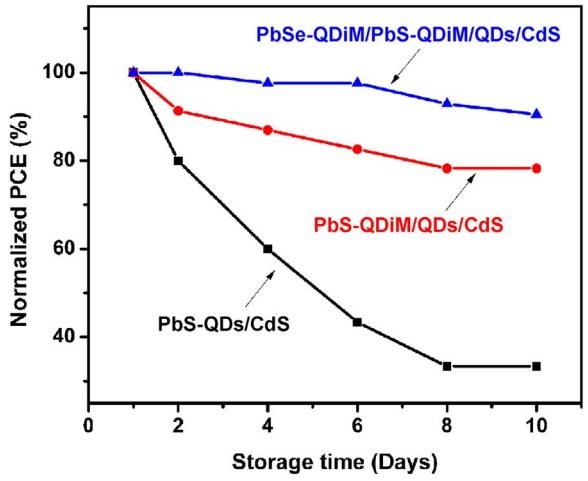

Fig. 10. long-term stability assessment of CBD-PbS/CdS solar cells with different assembled structures.

PbS and PbSe-QDiM are about 200, 1000 and 1000 nm, respectively.

Considering the stability factor for commercialization, we found that the utilization of QDiM absorber layers can not only significantly increase the PEC, but also improve the device stability. Only 10% performance degradation was observed from PbSe/PbS triple-tandem stacked solar cells over 10 days storage time in ambient at room temperature, comparing with the 67% degradation on the CBD-PbS QDs solar cells, as shown in Fig. 10. One of the possible reasons for improved stability could be due to the higher electron affinities of the micro-matrix, which are less reactive and hence, less susceptible to performance degrading reactions [16,30,31].

4. Conclusions

In summary, we have proposed and demonstrated a low-cost, three layer stacked solar cell involved the Pb-chalcogenide QDs and QDiM using the CBD method. The morphologies of PbS and PbSe layers could be precisely tailored just by controlling the CBD growth temperature and complex agents. The device showed a PCE enhancement of 4.2% due to the increased J_{sc} of 40 mA/cm^2. Such increase is the result of the smooth carrier transportation and the extend absorption covering both visible and near-infrared regions, while reminding a relatively large V_{oc} of 0.28 eV. We envision that PCE will be further increased by optimizing the device structural parameters, such as the fill factor.

Acknowledgements

The authors thank Mr. Yang Cheng and Dr. Vincent Whiteside from Professor Ian Sellers's group in Physics Department of University of Oklahoma for their help in measuring the visible-NIR PL spectra and I-V measurement using their solar simulator. The authors also thank Dr. Preston Larson for his help in SEM measurements. This work is partially supported by the US Army Research Office (ARO) and Oklahoma Center for the Advancement of Science and Technology (OCAST) under Grant No. W911NF-14-1-0312 and AR14-035, AR132-003.

Appendix A. Supporting information

Supplementary data associated with this article can be found in the online version at http://dx.doi.org/10.1016/j.solmat.2017.07.025.

References

[1] S.A. McDonald, G. Konstantatos, S. Zhang, P.W. Cyr, E.J.D. Klem, L. Levina, E.H. Sargen, Solution-processed PbS quantum dot infrared photodetectors and photovoltaics, Nat. Mater. 4 (2005) 138–142.
[2] D.Y. Kim, K.R. Choudhury, J.W. Lee, D.W. Song, G. Sarasqueta, F. So, PbSe nanocrystal-based infrared-to-visible up-conversion device, Nano Lett. 11 (2011) 2109–2113.
[3] J.R. Manders, T.H. Lai, Y. An, W. Xu, J. Lee, Do.Y. Kim, G. Bosman, F. So, Low-noise multispectral photodetectors made from all solution-processed inorganic semiconductors, Adv. Funct. Mater. 24 (2014) 7205–7210.
[4] G.H. Carey, A.L. Abdelhady, Z. Ning, S.M. Thon, O.M. Bakr, E.H. Sargent, Colloidal quantum dot solar cells, Chem. Rev. 115 (2015) 12732–12763.
[5] R.J. Ellingson, M.C. Beard, J.C. Johnson, P. Yu, O.I. Micic, A.J. Nozik, A. Shabaev, A.L. Efros, Highly efficient multiple exciton generation in colloidal PbSe and PbS quantum dots, Nano Lett. 5 (2005) 865–871.
[6] A.G. Midgett, J.M. Luther, J.T. Stewart, D.K. Smith, L.A. Padilha, V.I. Klimov, A.J. Nozik, M.C. Beard, Size and composition dependent multiple exciton generation efficiency in PbS, PbSe, and $PbSxSe_{1-x}$ alloyed quantum dots, Nano Lett. 13 (2013) 3078–3085.
[7] J. Zhang, J. Gao, C.P. Church, E.M. Miller, J.M. Luther, V.I. Klimov, M.C. Beard, Nano Lett. 14 (2014) 6010–6015.
[8] D.J. Milliron, PbSe quantum dot solar cells with more than 6% efficiency fabricated in ambient atmosphere, Nat. Mater. 13 (2014) 772–773.
[9] O.E. Semonin, J.M. Luther, S. Choi, H.Y. Chen, J. Gao, A.J. Nozik, M.C. Beard, Peak external photocurrent quantum efficiency exceeding 100% via MEG in a quantum dot solar cell, Science 334 (2011) 1530–1533.
[10] C.-H.M. Chuang, P.R. Brown, V. Bulovic, M.G. Bawendi, Nat. Mater. 13 (2014) 796–801.
[11] X. Lan, S. Masala, E.H. Sargent, Charge-extraction strategies for colloidal quantum dot photovoltaics, Nat. Mater. 13 (2014) 233–240.
[12] J. Tang, K.W. Kemp, S. Hoogland, K.S. Jeong, H. Liu, L. Levina, M. Furukawa, X. Wang, R. Debnath, D. Cha, K.W. Chou, A. Fischer, A. Amassian, J.B. Asbury, E.H. Sargent, Colloidal-quantum-dot photovoltaics using atomic-ligand passivation, Nat. Mater. 10 (2011) 765–771.
[13] J. Hernandez-Borja, Y.V. Vorobiev, R. Ramirez-Bon, Thin film solar cells of CdS/PbS chemically deposited by anammoniafree, process, Sol. Energy Mater. Sol. Cells 95 (2011) 1882–1888.
[14] A.S. Obaid, Z. Hassan, M.A. Mahdi, M. Bououdina, Fabrication and characterisations of n-CdS/p-PbS heterojunction solar cells using microwave-assisted chemical bath deposition, Sol. Energy 89 (2013) 143–151.
[15] D.H. Yeon, S.M. Lee, Y.H. Jo, J.H. Moon, Y.S. Cho, Origin of the enhanced photovoltaic characteristics of PbS thin film solar cells processed at near room temperature, J. Mater. Chem. A 2 (2014) 20112–20117.
[16] D.H. Yeon, B.C. Mohanty, S.M. Lee, Y.S. Cho, Effect of band-aligned double absorber layers on photovoltaic characteristics of chemical bath deposited PbS/CdS thin film solar cells, Sci. Rep. 5 (2015) 14353–14357.
[17] T. Safrani, T.A. Kumar, M. Klebanov, N. Arad-Vosk, R. Beach, A. Saar, I. Abdulhalim, G. Sarusi, Y. Golan, Chemically deposited PbS thin film photo-conducting layers for optically addressed spatial light modulators, J. Mater. Chem. C 2 (2014) 9132–9140.
[18] S. Sengupta, M. Perez, A. Rabkin, Y. Golan, In situ monitoring the role of citrate in chemical bath deposition of PbS thin films, CrystEngComm 18 (2016) 149–156.
[19] S. Gorer, A. Albu-Yaron, G. Hodes, Chemical solution deposition of lead selenide films: a mechanistic and structural study, Chem. Mater. 7 (1995) 1243–1256.
[20] L. Fan, P. Wang, Q. Guo, H. Han, M. Li, Z. Chen, H. Zhao, D. Zhang, Z. Zheng, J. Yang, Ultrasound-modulated microstructure of PbS film in ammonia-free chemical bath deposition, RSC Adv. 5 (2015) 10018–10025.
[21] G. Hodes, Semiconductor and ceramic nanoparticle films deposited by chemical bath deposition, Phys. Chem. Chem. Phys. 9 (2007) 2181–2196.
[22] M. Gloecklera, J.R. Sites, J. Appl. Phys. 95 (2004) 4438–4445.
[23] S. Sridaran, A. Chavan, P. Dutta, Appl. Phys. Lett. 89 (2006) 142116.
[24] S.A. McDonald, P.W. Cyr, L. Levina, E.H. Sargent, Appl. Phys. Lett. 85 (2004) 2089–2091.
[25] J. Lee, E.V. Shevchenko, D.V. Talapin, J. Am. Chem. Soc. 130 (2008) 9673–9675.
[26] C.H. Jo, J.H. Kim, J. Kim, J.N. Kim, M.S. Oh, M.S. Kang, M.G. Kim, Y.H. Kim, B.K. Ju, S.K. Park, J. Mater. Chem. C 2 (2014) 10305–10311.
[27] B. Weng, J. Qiu, L. Zhao, C. Chang, Z. Shi, Appl. Phys. Lett. 104 (2014) 121111–121115.
[28] A. Lipovskii, E. Kolobkova, V. Petrikov, Synthesis and characterization of PbSe quantum dots in phosphate glass, Appl. Phys. Lett. 71 (1997) 3406–3408.
[29] Roland Scheer, Hans-Werner Schock, Chalcogenide Photovoltaics: Physics, Technologies, and Thin Film Devices, Wiley-VCH Verlag GmbH & Co., 2011.
[30] J.D. Levine, Nodal hydrogenic wave functions of donors on semiconductor surfaces, Phys. Rev. 140 (1965) A586–A589.
[31] Eric T. Hoke, I.T. Sachs-Quintana, Matthew T. Lloyd, Isaac Kauvar, William R. Mateker, Alexandre M. Nardes, Craig H. Peters, Nikos Kopidakis, Michael, D. McGehee, The role of electron affinity in determining whether fullerenes catalyze or inhibit photooxidation of polymers for solar cells, Adv. Mater. 2 (2012) 1351–1357.